Isostaticity at Frictional Jamming

Stefanos Papanikolaou,[1,2] Corey S. O'Hern,[1,2,3] and Mark D. Shattuck[4]

[1]*Departments of Mechanical Engineering & Materials Science, Yale University, New Haven, Connecticut 06520, USA*
[2]*Department of Physics, Yale University, New Haven, Connecticut 06520, USA*
[3]*Department of Applied Physics, Yale University, New Haven, Connecticut 06520, USA*
[4]*Benjamin Levich Institute and Physics Department, The City College of the City University of New York, New York, New York 10031, USA*

(Received 24 July 2012; published 7 May 2013)

Amorphous packings of frictionless, spherical particles are isostatic at jamming onset, with the number of constraints (contacts) equal to the number of degrees of freedom. Their structural and mechanical properties are controlled by the interparticle contact network. In contrast, amorphous packings of frictional particles are typically hyperstatic at jamming onset. We perform extensive numerical simulations in two dimensions of the geometrical asperity (GA) model for static friction to further investigate the role of isostaticity. In the GA model, interparticle forces are obtained by summing up purely repulsive central forces between periodically spaced circular asperities on contacting grains. We compare the packing fraction, contact number, mobilization distribution, and vibrational density of states (in the harmonic approximation) using the GA model to those generated using the Cundall-Strack approach. We find that static packings of frictional disks obtained from the GA model are mechanically stable and *isostatic* when we consider interactions between asperities on contacting particles. The crossover in the structural and mechanical properties of static packings from frictionless to frictional behavior as a function of the static friction coefficient coincides with a change in the type of interparticle contacts and the disappearance of a peak in the density of vibrational modes for the GA model. These results emphasize that mesoscale features of the model for static friction play an important role in determining the properties of granular packings.

DOI: 10.1103/PhysRevLett.110.198002 PACS numbers: 45.70.−n, 46.55.+d, 61.43.−j, 63.50.−x

Recently, intense effort has been devoted to understanding the jamming transition of athermal frictionless spheres with repulsive contact interactions [1–4]. However, physical models of granular media should include static friction [5]. Experiments [6,7] and simulations [8–10] have shown that amorphous frictional sphere packings can be obtained at jamming onset over a wide contact number range $d+1 \leq z \leq 2d$ [3,11,12], where d is the spatial dimension. In addition, a crossover from frictionless random close packing $\phi \simeq \phi_{\mathrm{RCP}}$ and $z \simeq 2d$ to frictional random loose packing $\phi \simeq \phi_{\mathrm{RLP}}$ and $z \simeq d+1$ occurs as the static friction coefficient μ increases above $\mu^* \sim 0.1$ (0.01) in $d = 2(3)$ [12]. Moreover, a large number N_s of "sliding" contacts (with the tangential equal to the normal force times μ) exists for small μ, and N_s decreases with increasing μ [12,13]. When contact-counting arguments account for sliding contacts, frictional packings can be described as "isostatic" with vibrational properties similar to those of frictionless spheres [10].

In this Letter, we address several open questions: How sensitive are the structural (dependent on particle positions) and mechanical properties (dependent on interparticle forces) of frictional packings to the friction model employed? What determines the static friction coefficient μ^* that marks the crossover from frictionless to frictional behavior for static packings? How does $D(\omega)$ for frictional packings differ from that for frictionless particles with complex and anisotropic (e.g., convex and nonconvex) shapes?

Most prior studies focused on the Cundall-Strack (CS) approach [14], where static friction is modeled by a tangential spring (with spring constant k_t and restoring force $k_t u_t$, where u_t is the relative tangential displacement) when particles are in contact, and the Coulomb sliding condition holds. With the GA model, we can distinguish interparticle contacts based on which asperities interact and calculate $D(\omega)$ by taking derivatives of total potential energy without making *ad hoc* assumptions for sliding contacts [10]. Prior GA models mimicking frictional interactions [15–17] studied dense granular flows.

Static GA packings are mechanically stable (MS) and *isostatic* when asperity interactions are considered, independent of the effective static friction coefficient. The crossover in the structural and mechanical properties as a function of the effective friction coefficient coincides with changes in the interaction types between asperities and the disappearance of a strong, primarily rotational peak in $D(\omega)$ at low frequency. We find that $D(\omega)$ for the GA model differs from analogous studies for the CS case [10].

We construct MS packings of N rough bidisperse disks (50-50 by number with diameter ratio $r = 1.4$) in $d = 2$ using the GA model and compare them to those from the CS approach. The lower right panel of Fig. 1 shows rough circular disks in the GA model, characterized by N_a

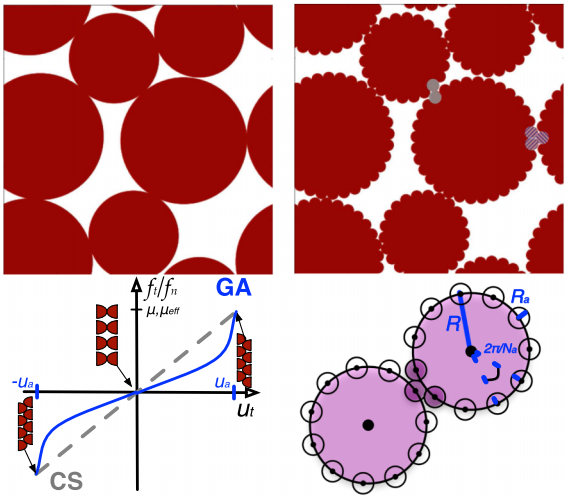

FIG. 1 (color online). Top: Nearly identical MS packings of $N = 6$ bidisperse disks at jamming onset from the CS (left) and GA (right) models with μ, $\mu_{\rm eff} \simeq 0.3$ and $\phi_J \simeq 0.78$ and 0.76, respectively; they possess the same nine interparticle contacts, and the GA model has the isostatic number of contacting asperities $N_c^{aa} = 3N - 1 = 17$. (right) The central particle has five interactions between asperities on three contacting grains. The solid and striped gray contacts between the central particle and its neighbors are single and double asperity contacts, respectively. Bottom: (left) Schematic of the ratio of tangential and normal forces f_t/f_n at constant interparticle overlap versus the relative tangential displacement u_t for the CS (dashed) and GA (solid) models. For CS, f_t/f_n is linear with slope k_t, whereas for GA $f_t/f_n = u_t/[(\sigma_{ij}^{aa'} - r_{ij}^{aa'})^2 - u_t^2]^{1/2}$, where $r_{ij}^{aa'}$ is constant at fixed overlap. Single (double) asperity contacts occur near $f_t/f_n = 0$ (maximal $|f_t|/f_n$). Sliding happens when $\pm u_a = \pm \mu f_n/k_t$ in CS, whereas in GA $u_a = \pm \sigma_{ij}^{aa'}/(2\sqrt{1 + 1/\mu_{\rm eff}^2})$ and f_t/f_n is periodic at zero overlap. (right) Schematic of the interaction in the GA model between disks with radius R, N_a circular asperities with radius R_a and angle $2\pi/N_a$.

circular asperities with centers on the disk rim and ratio of the asperity to particle radius R_a/R. We consider two disk interactions: (1) asperities on disks i and j and (2) the core of i with an asperity on j. All interactions are purely repulsive linear springs [3]. Asperities a and a' on disks i and j interact through $V_{ij}^{aa'} = \epsilon/(2\sigma_{ij}^2)(\sigma_{ij}^{aa'} - r_{ij}^{aa'})^2\Theta(1 - r_{ij}^{aa'}/\sigma_{ij}^{aa'})$, where $r_{ij}^{aa'}$ is the center-to-center separation between asperities, $\sigma_{ij}^{aa'} = R_i^a + R_j^{a'}$, and $\sigma_{ij} = \sigma_{ij}^{aa'} + R_i + R_j$. We locate asperity a on the rim of disk i at angle $\theta_i^a = \theta_i + 2\pi a/N_a$ and coordinates $\mathbf{r}_i^a = \mathbf{r}_i + R_i(\cos\theta_i^a, \sin\theta_i^a)$, where $\mathbf{r}_i$ is the position of disk i. Asperity a on disk i and core of j interact through $V_{ij}^a = \epsilon/(2\sigma_{ij}^2)(\sigma_{ij}^a - r_{ij}^a)^2\Theta(1 - r_{ij}^a/\sigma_{ij}^a)$, where $\sigma_{ij}^a = R_i^a + R_i + R_j$ (where r_{ij}^a is the separation between the center of asperity a on i and the center of j). The total GA potential energy is $V = \sum_{i>j}\sum_{a>a'} V_{ij}^{aa'} + \sum_{i>j}\sum_a V_{ij}^a$.

We can define an effective GA static friction coefficient $\mu_{\rm eff} = 1/\sqrt{[(2R_a/R)/\sin(\pi/N_a)]^2 - 1}$, the maximum tangential to normal interparticle force ratio, when an asperity on disk i fits in between two adjacent asperities on j as in the lower right panel of Fig. 1. This is the maximum tangential to normal force ratio in the zero interparticle overlap limit. The ratio of the number of asperities on the large and small particles is set close to r so that the interspecies $\mu_{\rm eff}$ is approximately the same as the intraparticle one. The CS [4,12] static friction is included between geometrically smooth circular disks i and j using a tangential spring with tangential to normal spring constant ratio $k_t/k_n = 1/3$ ($k_n = \epsilon/\sigma_{ij}$) [5], and $|f_t|$ remains at the maximum value μf_n when u_t exceeds the Coulomb threshold. We studied system sizes from $N = 6$ to 96, asperity numbers $N_a = 8$, 16, and 32, and μ, $\mu_{\rm eff} = 10^{-3}$ to 10.

We generate approximately 10^5 MS GA and CS packings at jamming onset, for each N and μ or $\mu_{\rm eff}$, using the compressive quench from zero density simulation protocol [18]. We randomly place point particles in a square periodic cell of unit size. We increase particle radii in small steps corresponding to $\Delta\phi = 10^{-4}$. After each $\Delta\phi$ increment, the system is relaxed to the nearest local potential energy minimum using dissipative forces proportional to the disks' translational and angular velocities with large damping coefficients. If after minimization we have zero total potential energy per particle (i.e., $V/N < V_{\rm tol}/\epsilon = 10^{-14}$), we continue compressing the system. Otherwise, if $V/N \geq V_{\rm tol}/\epsilon$, we decompress. $\Delta\phi$ is halved each time we switch from compression to decompression or vice versa. We stop when $V_{\rm tol} < V/N < 1.01V_{\rm tol}$ and the average particle overlap is less than 10^{-7}. All GA packings are mechanically stable with $3N' - 2$ eigenvalues $m_i > 0$ for the dynamical matrix $M_{kl} = d^2V/(d\mathbf{R}_k d\mathbf{R}_l)$, where $\mathbf{R} = \{\mathbf{r}_1, \ldots, \mathbf{r}_{N'}, (R_1 + R_1^a)\theta_1, \ldots, (R_{N'} + R_{N'}^a)\theta_{N'}\}$, $N' = N - N_r$, and N_r represents the rattler particles. (CS and GA rattler particles have less than three interparticle contacts.) Figure 2 shows results for the average packing fraction $\langle\phi_J\rangle$ and contact number $\langle z_{pp}\rangle = \langle 2N_{pp}/(N')\rangle$ at jamming onset, where N_{pp} are the particle-particle contacts irrespective of the number of asperity contacts. As previously noted [12], $\langle\phi_J\rangle$ varies from ≈ 0.84 to 0.75 and $\langle z_{pp}\rangle$ ranges from ≈ 4 to 3 as μ increases for both CS and GA models. The crossover from frictionless to frictional behavior occurs near $\mu^* \approx 0.1$. $\langle\phi_J\rangle$ is 1% larger at large $\mu_{\rm eff}$ values for the GA model, as expected for finite N_a. The upper-right panel of Fig. 2 shows N_r/N versus μ or $\mu_{\rm eff}$. Both increase with μ or $\mu_{\rm eff}$ and then plateau. Because of slow relaxation processes, we detect fewer rattlers for the GA model, causing $\langle z_{pp}\rangle$ to be 5% larger at large $\mu_{\rm eff}$.

The cumulative mobilization distributions [$A(\zeta) = \int_0^\zeta P(x)dx$, where $\zeta = |f_t|/(\mu f_n)$] are qualitatively similar for the CS and GA models in Fig. 3. At low μ or $\mu_{\rm eff}$, $A(\zeta)$ for both models has a strong peak at $\zeta = 1$ [9,13]. As μ or

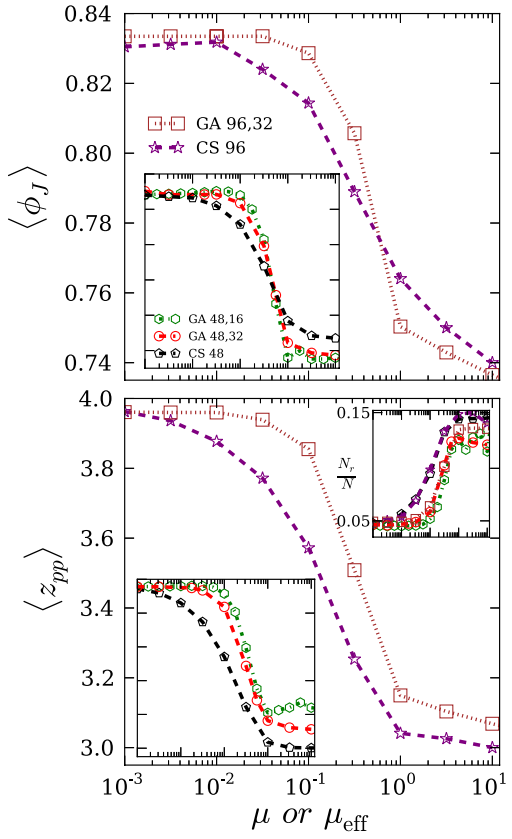

FIG. 2 (color online). Top: Average packing fraction $\langle \phi_J \rangle$ for MS packings from the CS and GA models versus μ or $\mu_{\rm eff}$. The lower-left inset shows $\langle \phi_J \rangle$ versus μ or $\mu_{\rm eff}$ for several system sizes N and asperity numbers N_a. Legends show N_a (right) and N (left), and axes without tick labels are the same as in the main panel. Bottom: Average interparticle contact number $\langle z_{pp} \rangle$ versus μ or $\mu_{\rm eff}$. The insets show the N and N_a dependence of $\langle z_{pp} \rangle$ (lower left) and rattler fraction N_r/N (upper right).

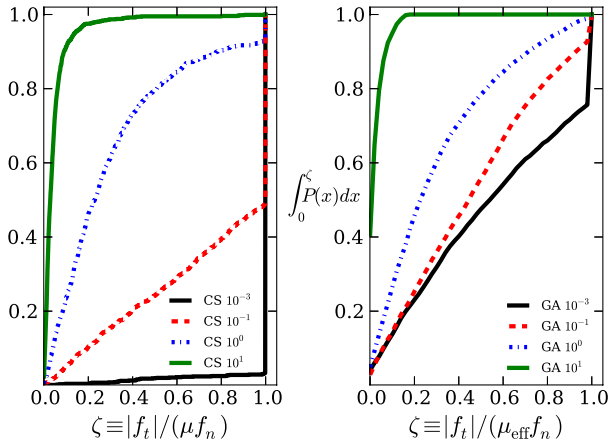

FIG. 3 (color online). Cumulative mobilization distributions for $N = 48$ for the CS (left) and GA (right) models for μ, $\mu_{\rm eff} = 10^{-3}$, 10^{-1}, 1, and 10, where the mobilization $\zeta = |f_t|/(\mu f_n)$. GA mobilities $\zeta > 1$ can occur due to finite interparticle overlaps. The bin at $\zeta = 1$ includes all $\zeta \geq 1$ to allow a comparison with the CS model.

$\mu_{\rm eff}$ increases, it disappears and the average mobilization decreases. Only quantitative differences in the mobilization distributions arise from different tangential force laws shown in the lower-left panel of Fig. 1. At fixed overlap, f_t/f_n varies linearly with u_t until the sliding limit at $\pm u_a$, whereas f_t/f_n is periodic for the GA model.

In the lower panel of Fig. 4, we show the asperity contacts (single, double, and triple) for each interparticle contact. We find that MS packings are *isostatic* [19] with $N_c^{aa} = 3N' - 1$ contacts over the entire range of $\mu_{\rm eff}$. Deviations from isostaticity are less than 2% for all N and N_a values studied. In contrast, static packings of frictional particles are hyperstatic ($z_{pp} > 3$) when considering interparticle contacts for both GA and CS [4] (cf. lower panel of Fig. 2).

Asperity contacts may explain the structural and mechanical crossover near μ^*. In the top panel of Fig. 4, we plot the probability of single and double asperity contacts versus $\mu_{\rm eff}$. They are roughly equiprobable at low friction, whereas only double asperity contacts occur at high friction. To maintain isostaticity, at low friction there are typically two double and two single asperity contacts per particle, whereas at high friction three double contacts form for a total of approximately six per particle in both cases. The $\mu_{\rm eff}$ value where single become less probable than double asperity contacts (~ 0.1), coincides with the μ^* value above which the packing fraction, contact number, and mobilization distributions begin to deviate significantly from frictionless behavior. Similar behavior also occurs for the CS model. In the upper panel of Fig. 4, we show the probability of low ($\zeta < \zeta_c = 0.5$) and high ($\zeta \geq \zeta_c$) mobilization contacts versus μ. (The results do not depend strongly on ζ_c.) At low friction, most contacts possess high mobilization, whereas they have low mobilization at high friction. At high friction, double asperity contacts resemble low mobilization contacts. At low friction, both single and double asperity contacts can possess high mobilization. The crossover in the probabilities of low and high mobilization contacts occurs also near μ^*.

We can directly calculate the GA $D(\omega)$ from the total potential energy (in the harmonic approximation). The eigenmode with frequency ω_j is $\hat{\mathbf{m}}_j = \{m_j^{x,1}, m_j^{y,1}, m_j^{\theta,1}, \ldots, m_j^{x,N'}, m_j^{y,N'}, m_j^{\theta,N'}\}$ with $\sum_{\lambda,i}(m_j^{\lambda,i})^2 = 1$. The rotational R_j and translational T_j content of each mode j are $T_j = \sum_{i=1,N'}\sum_{\lambda=x,y}(m_j^{\lambda i})^2$, and $R_j = 1 - T_j$; the participation ratio $P_j = [\sum_{\lambda,i}(m_j^{\lambda,i})^2]^2/[N\sum_{\lambda,i}(m_j^{\lambda,i})^4]$ for $\lambda = x$, y and θ separately, and the optical order parameter $Q_j^{\rm opt} = \sum_{i,k} m_j^{\theta,i} m_j^{\theta,k}/[N\sum_i (m_j^{\theta,i})^2]$ that characterizes whether the rotational content of j is co- or counter-rotating [10].

$D(\omega)$ for MS packings using the GA model is shown in Fig. 5, with the following characteristics: (i) We observe a strong peak at low frequency whose height $D(\omega_{\rm max})$ increases

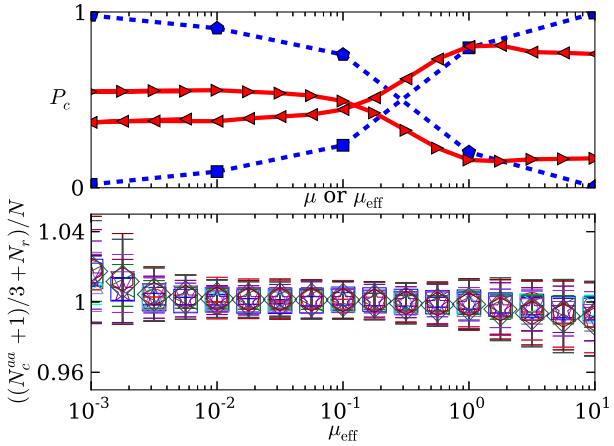

FIG. 4 (color online). Top: Probability P_c of different contact types versus μ or $\mu_{\rm eff}$. Contacts can be single (rightward triangles) and double asperity (leftward triangles) or low (squares) and high mobilization (pentagons) with $\zeta < \zeta_c = 0.5$ and $\zeta \geq \zeta_c$, respectively, for GA (solid red lines) and CS models (blue dashed lines). Bottom: The average isostaticity parameter $\langle\alpha\rangle = \langle[(N_c^{aa}+1)/3+N_r]/N\rangle$, where N_c^{aa} is the total number of asperity contacts, versus $\mu_{\rm eff}$ for several N and N_a. ($N = 6$ and $N_a = 16$, circles; 6 and 32, squares; 12 and 16, rightward triangles; 12 and 32, leftward triangles; 24 and 16, upward triangles; 24 and 32, downward triangles; 48 and 16, stars; 48 and 32, hexagons.) $\alpha = 1$ indicates an isostatic number of asperity contacts.

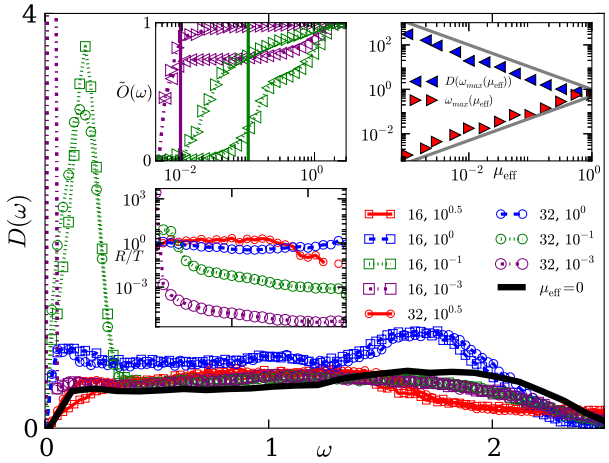

FIG. 5 (color online). $D(\omega)$ for $N = 48$, $N_a = 16$ and 32, and $\mu_{\rm eff} = 10^{-3}$, 10^{-1}, 1, and $10^{0.5}$ for the GA model. The area under $D(\omega)$ is the number of nonzero modes, $3N' - 2$, and $2N' - 2$ for $\mu_{\rm eff} = 0$. The upper-left inset shows $\tilde{O}(\omega)$ after simple shear (rightward triangles) and compression (leftward triangles) perturbations at high and low friction (different colors in main legend). Vertical solid lines indicate corresponding locations of the $D(\omega)$ peak. Lower-left inset shows R/T for the modes on a linear frequency scale. The upper-right inset tracks $\omega_{\rm max}$ and $D(\omega_{\rm max})$ for the low-frequency peak in $D(\omega)$ versus $\mu_{\rm eff}$ for $N_a = 32$. Solid lines have slopes -1 and 1.

and location $\omega_{\rm max}$ shifts to lower frequency with decreasing $\mu_{\rm eff}$. We find that $\omega_{\rm max} \sim \mu_{\rm eff}$ and $D(\omega_{\rm max}) \sim \mu_{\rm eff}^{-1}$ as $\mu_{\rm eff} \to 0$ (cf. upper-right inset of Fig. 5). These modes are mostly rotational ($R \sim 1$), globally incoherent ($Q^{\rm opt} \sim 0$), and quasilocalized ($P \lesssim 0.1$) as $\mu_{\rm eff} \to 0$. Similar peaks in $D(\omega)$ that contain low-frequency rotational modes have been found in ellipse packings [20,21] at low aspect ratio. For small $\mu_{\rm eff}$ as ω increases, $D(\omega)$ approaches the frictionless case with translational and quasilocalized modes at high frequencies. (ii) A peak in $D(\omega)$ at low frequency with $R \sim 1$ disappears for $\mu_{\rm eff} \gtrsim \mu^*$. (iii) For $\mu_{\rm eff} \gtrsim \mu^*$, modes have mixed rotational and translational content with $R \sim T$ at all frequencies. At low frequencies, modes are gearlike [22–24] ($Q_{\rm opt} \sim -0.5$) and collective ($P \sim 0.3$). At high frequencies, modes are increasingly localized with corotating angular components ($Q_{\rm opt} \sim 0.5$).

Low-frequency rotational modes couple strongly to the mechanical response of GA packings, shown by quasistatic (a) isotropic compression in packing fraction increments to $\Delta\phi_{\rm tot} = 10^{-8}$ or (b) simple shear in strain increments (coupled with Lees-Edwards boundary conditions) to $\gamma_{\rm tot} = 10^{-8}$ from a reference configuration at $\Delta\phi_0 = 10^{-6}$. We calculated the overlap $O(\omega) = \delta\mathbf{D} \cdot \hat{\mathbf{m}}_j(\omega)/|\delta\mathbf{D}|^2$ of the deformation vector $\delta\mathbf{D} \equiv \mathbf{D} - \mathbf{D}_0$, where $\mathbf{D}_0$ ($\mathbf{D}$) is the $3N'$-dimensional coordinate vector of the reference configuration [25]. In the upper inset of Fig. 5, the low-frequency rotational modes contribute to at least half of the cumulative and averaged absolute overlap $\tilde{O}(\omega) = \int_0^\omega |O(\omega')|d\omega' / \int_0^\infty |O(\omega')|d\omega'$ for both compression and shear.

Support from NSF Grant No. CBET-0968013 (M. S.) and DTRA Grant No. 1-10-1-0021 (S. P. and C. O.) is acknowledged. This work also benefited from the facilities and staff of the Yale University Faculty of Arts and Sciences High Performance Computing Center and NSF Grant No. CNS-0821132 that partially funded acquisition of the computational facilities. We thank T. Bertrand, K. Kumar, D. Kwok, M. Wang, and C. Schreck for their invaluable insights and comments throughout the course of this work.

[1] S. Torquato and F. H. Stillinger, Rev. Mod. Phys. **82**, 2633 (2010).
[2] A. J. Liu and S. R. Nagel, Nature (London) **396**, 21 (1998).
[3] C. S. O'Hern, L. E. Silbert, A. J. Liu, and S. R. Nagel, Phys. Rev. E **68**, 011306 (2003).
[4] M. van Hecke, J. Phys. Condens. Matter **22**, 033101 (2010).
[5] J. Shäfer, S. Dippel, and D. Wolf, J. Phys. I (France) **6**, 5 (1996).
[6] T. S. Majmudar and R. P. Behringer, Nature (London) **435**, 1079 (2005).
[7] D. Bi, J. Zhang, B. Chakraborty, and R. Behringer, Nature (London) **480**, 355 (2011).
[8] C. Song, P. Wang, and H. A. Makse, Nature (London) **453**, 629 (2008).

[9] L. E. Silbert, D. Ertaş, G. S. Grest, T. C. Halsey, and D. Levine, Phys. Rev. E **65**, 031304 (2002).
[10] S. Henkes, M. van Hecke, and W. van Saarloos, Europhys. Lett. **90**, 14003 (2010).
[11] S. F. Edwards and D. V. Grinev, Phys. Rev. Lett. **82**, 5397 (1999).
[12] L. E. Silbert, Soft Matter **6**, 2918 (2010).
[13] K. Shundyak, M. van Hecke, and W. van Saarloos, Phys. Rev. E **75**, 010301 (2007).
[14] P. A. Cundall and O. Strack, Geotechnique **29**, 47 (1979).
[15] S. A. Galindo-Torres, F. Alonso-Marroquin, Y. C. Wang, D. Pedroso, and J. D. Muñoz Castaño, Phys. Rev. E **79**, 060301(R) (2009).
[16] F. Alonso-Marroquin, Europhys. Lett. **83**, 14001 (2008).
[17] V. Buchholtz and T. Pöschel, Physica (Amsterdam) **202A**, 390 (1994).
[18] G.-J. Gao, J. Bławzdziewicz, and C. S. O'Hern, Phys. Rev. E **74**, 061304 (2006).
[19] A. Donev, S. Torquato, and F. H. Stillinger, Phys. Rev. E **71**, 011105 (2005).
[20] C. F. Schreck, N. Xu, and C. S. O'Hern, Soft Matter **6**, 2960 (2010).
[21] C. F. Schreck, M. Mailman, B. Chakraborty, and C. S. O'Hern, Phys. Rev. E **85**, 061305 (2012).
[22] R. Mahmoodi Baram, H. J. Herrmann, and N. Rivier, Phys. Rev. Lett. **92**, 044301 (2004).
[23] H. J. Herrmann, G. Mantica, and D. Bessis, Phys. Rev. Lett. **65**, 3223 (1990).
[24] G. Oron and H. Herrmann, J. Phys. A **33**, 1417 (2000).
[25] See Supplemental Material at http://link.aps.org/supplemental/10.1103/PhysRevLett.110.198002 for a detailed description of the numerical procedure used for the overlap calculation.